



Prediction of dose distribution from luminescence image of water using a deep convolutional neural network for particle therapy

A short running title: Dose prediction by DCNN for luminescence

Takuya Yabe¹⁻²⁾, Seiichi Yamamoto^{1)*}, Masahiro Oda³⁾, Kensaku Mori³⁾, Toshiyuki Toshito⁴⁾, Takashi Akagi⁵⁾

¹⁾ Radiological and Medical Laboratory Sciences, Nagoya University Graduate School of Medicine, Nagoya, Japan,

²⁾ Department of Medical Technology, Nagoya University Hospital, Nagoya, Japan,

³⁾ Graduate School of Informatics, Nagoya University, Nagoya, Japan,

⁴⁾ Nagoya Proton Therapy Center, Nagoya City West Medical Center, Nagoya, Japan,

⁵⁾ Hyogo Ion Beam Medical Center, Tatsuno, Japan,

*Corresponding author: Seiichi Yamamoto

1-1-20 Daiko-Minami, Higashi-ku, Nagoya, Japan, 461-8673

Tel: +81-52-719-1559, e-mail: s-yama@met.nagoya-u.ac.jp

ABSTRACT

Purpose: We recently obtained nearly the same depth profiles of luminescence images of water as dose for protons by subtracting the Cerenkov light component emitted by secondary electrons of prompt gamma photons. However, estimating the distribution of Cerenkov light with this correction method is time consuming, depending on the irradiated energy of protons by Monte Carlo simulation. Therefore, we proposed a method of estimating dose distributions from the measured luminescence images of water using a deep convolutional neural network (DCNN).

This article has been accepted for publication and undergone full peer review but has not been through the copyediting, typesetting, pagination and proofreading process, which may lead to differences between this version and the [Version of Record](#). Please cite this article as [doi: 10.1002/MP.14372](https://doi.org/10.1002/MP.14372)

This article is protected by copyright. All rights reserved

Methods: In this study, we adopted the U-Net architectures as the DCNN. To prepare a large amount of image data for DCNN training, we calculated the training data pairs of 2D-dose distributions and luminescence images of water by Monte Carlo simulation for protons and carbon ions. After training the U-Net model for protons or carbon ions using these dose distributions and luminescence images calculated by Monte Carlo simulation, we predicted the dose distributions from the calculated and measured luminescence images of water using the trained U-Net model.

Results: All of the U-Net model's predicted images were in good agreement with the MC-calculated dose distributions and showed lower values of the root mean square percentage error (RSMPE) and higher values in the structural similarity index (SSIM) in comparison with these values for calculated or measured luminescence images.

Conclusion: We confirmed that the DCNN effectively predicts dose distributions in water from the measured as well as calculated luminescence images of water for particle therapy.

Keywords: deep convolutional neural network; luminescence of water; particle therapy; Cerenkov light

1. Introduction

For range estimation during or after particle-beam irradiation, attempts are being made to image the irradiated particle-beam dose distribution and its location especially with respect to depth in the measurement phantom. For one of these trials, imaging of the induced positrons by particle-beam irradiation is conducted using positron emission tomography or gamma cameras [1-4]. Detecting the prompt gamma photons [5-6] or imaging of the prompt X-rays [7-8] emitted during particle-beam irradiation have also been conducted for this purpose. These methods have the advantage of imaging the particle-beam dose distribution and its location from outside the subjects. Acoustic signal detection during particle-beam irradiation has also been tried for the beam range measurements [9-10].

As part of this imaging the particle-beam dose distributions and its locations, we recently imaged the luminescence of water using a cooled charge-coupled device (CCD) camera during the irradiation of protons [11] and carbon ions [12]. The luminescence of water is thought to be generated by the same mechanism as Cerenkov light, but produced at lower energy than the Cerenkov light threshold [13-14]. Although the images obtained with this method can only be measured with transparent materials such as water, the measured images showed the same ranges as those measured by an ionization chamber [11-12]. Furthermore, the images were similar to dose distributions [11-12]. However, with our careful observations of the images of protons, the depth profiles of the measured luminescence images showed smaller Bragg peak heights than those measured by an ionization chamber. Offset luminescence was also observed in the area behind the Bragg peak. Cerenkov light produced from the secondary electrons generated by the interaction of the prompt gamma photons with water caused this phenomenon [15]. For carbon ions, the luminescence image's depth profiles showed high intensity in the shallow area [12]. This high intensity was thought to be mainly due to the Cerenkov light emitted by secondary electrons whose energy was higher than the Cerenkov light threshold in the shallow area [12]. For protons, we corrected the depth profiles of the measured luminescence images of water by subtracting the simulated distributions of the Cerenkov light [15]. As a result, we obtained almost the same depth profiles as the dose for protons [15]. However, this correction method needs to estimate the Cerenkov light distribution by Monte Carlo simulation, which takes a long time to produce images. More than one day was required to produce the distribution for single energy by Monte Carlo simulation.

A deep learning approach with a deep convolutional neural network (DCNN) is an effective way to precisely predict the corrected images from noisy and distorted images. It was employed for generating transmission images of positron emission tomography (PET) from emission images [16-17] or removing artifacts from images [18-19]. A deep learning approach for a recurrent neural network (RNN) was also proposed to estimate depth doses from the activity data of proton-induced positron emitters and

successfully obtained one-dimensional (1D) depth doses from simulated data [20-21]. A similar approach was attempted for prompt gamma photon imaging using a Compton camera [22]. We found that these approaches are promising for the simulated and measured luminescence images of water during irradiation of protons or carbon ions to derive precise dose distributions shortly after training the neural network.

In this study, we propose a method of predicting two-dimensional (2D) dose distributions from the measured luminescence images of water for protons and carbon ions using a DCNN. This proposed method has two advantages. One is that we can predict the dose distribution from the measured luminescence images faster and simpler than with our previous method [15] because we do not need Monte Carlo simulation to predict the images after training the neural network. The other is that we can derive two-dimensional (2D) dose distributions as well as 1D-depth doses using DCNN. In this paper, we first calculated the 2D dose distributions and luminescence images of water by Monte Carlo simulation and trained the network using these data. Next, we predicted the dose distributions from the measured and calculated luminescence images using the trained U-Net model. Finally, we evaluated the accuracy of our method by comparing the U-Net predicted dose distributions with the dose distributions.

2. Materials and Methods

2.1 Monte Carlo simulation for DCNN training data

Deep learning approaches need a large amount of training data. However, preparing the training data for a variety of irradiation conditions takes a long time by imaging experiments. Thus, we calculated dose distributions and the luminescence images of water during irradiation of protons or carbon ions by Monte Carlo simulation to prepare a large amount of training data. We used the Geant4 ver.10.3 [23] as a Monte Carlo code because the optical photon processes (G4OpticalPhysics), Cerenkov light (G4Cerenkov), and scintillation photon generation (G4Scintillation) are included in the Geant4 class library. For our simulation,

we scored the deposited energy and generated the optical photon information in a water phantom. The water phantom used as the target was 200 mm (horizontal) \times 200 mm (vertical) \times 100 mm (width), which was identical to that used in the experiments on the luminescence imaging of water [11-12]. The simulated images had a pixel size of 1.04 mm, which is the same as the measured luminescence image, and all of the simulated data have images of 192 pixels \times 192 pixels. All of the calculated data made by Monte Carlo simulation were 2D images. The depth of the data was 32-bit.

For the luminescence imaging simulation, we calculated the images that had almost the same distributions as the measured luminescence images of water during proton and carbon-ion irradiation using the previously developed Monte Carlo simulation [15]. We calculated the luminescence of water images for different irradiated energies and positions using the Monte Carlo simulation. We used the scintillation photon-generation process as the method of light production from the luminescence of water at a lower energy than the Cerenkov light threshold. The produced photon light was \sim 0.1 photons/MeV for the luminescence of water. For the refractive index of water and the spectrum of luminescence of water, we used the same values as those in our previous study [15]. In the optical photon simulation, we scored the optical photons generated from the Cerenkov light generation process in the water phantom during the irradiation of the protons or carbon ions. The camera's lens (30 mm \times 30 mm) was located 40 cm from the phantom surface. We scored the position and the wavelength of the optical photons generated in the water phantom if their direction passed through the lens. We also considered the light transmission of the lens and the sensitivity profile of the CCD camera to fit the simulation to the experiments. We considered the light signal's blurring as a Gaussian filter because blurring leads to a broadening of the Bragg peak and a decrease in its height. We convolved all Monte Carlo (MC)-calculated luminescence image data by the Gaussian filter with one sigma to reproduce the CCD camera's measured image.

In all simulations, the physics lists of QGSP_BERT for the hadron process and G4EmStandardPhysics_opt3 for the electron-magnetic process were applied. In this physics package, the

production cut for the range of secondary particles (photons, electrons, positrons, and protons) was set to 0.1 mm to calculate the secondary electrons that exceed the Cerenkov light threshold (\sim 260 keV). To increase training data variations, we obtained the MC-calculated luminescence images for different positions of the camera's lens. The calculated luminescence images were generated by moving the camera position horizontally and vertically. We did not change the vertical axis (beam angle) and distances because luminescence imaging is usually conducted with a fixed irradiation angle and distance. The camera's lens position relative to the water phantom position was determined randomly. The simulation for the MC-calculated luminescence images consisted of 19 types of irradiated energies and 200 different lens positions. For the proton, the incident energies were from 60 MeV to 150 MeV at 5-MeV intervals. For carbon ions, the incident energies were from 170 MeV/u to 260 MeV/u at 5-MeV/u intervals. The beam shapes were Gaussian-shaped pencil beams for both protons and carbon ions. The lateral distributions used the beam-width data measured by an in-house CCD camera/fluorescent screen system for protons [24] and calculated by a treatment planning system for carbon ions. The number of primary histories was set to 1.0×10^7 particles for protons and 3.0×10^6 particles for carbon ions. All proton or carbon-ion beams were directed downwards and normally incident to the water surface.

2.2 Prediction of dose distributions from MC-calculated and measured luminescence images of protons or carbon ions using the U-Net model

2.2.1 DCNN model architecture

We adopted and modified the U-Net architecture proposed by Ronneberger et al. [25]. Our model's architecture is shown in Fig. 1. The architecture consists of an encoding process (left side) and a decoding process (right side). The encoding process consists of two 3×3 convolutional layers, each followed by a batch-normalization (BN), rectified-linear-units (ReLU) activation function and a 2×2 max pooling with stride two for down-sampling. The feature maps are copied and concatenated via the skip connections to

the convolutional layers at each down-sampling step. The decoding process consists of two 3×3 convolutional layers, up-sampling, concatenation with the copied feature map from the encoding process, and two 3×3 convolutions, each followed by BN and ReLU. In addition, a 1×1 convolutional layer with sigmoid as the activate function was applied as the output layer.

2.2.2 Network training

All MC-calculated images of protons or carbon ions used for the training were split into training data of 13 types of irradiated energies (2600 pairs), validation data of three types of irradiated energies (600 pairs), and testing data of three types of irradiated energies (600 pairs). Using the training data, the U-Net model was trained by minimizing the loss function defined as the mean square error (MSE) between the U-Net predicted dose distributions and the MC-calculated dose distribution. We built two U-Net models based on proton and carbon ion dataset. These models were implemented using *Keras* and *PlaidML* as a backend, and were trained on a Radeon Pro 580 graphic processing unit. The loss function was optimized by the Adam optimizer algorithm. The algorithm's parameters were set to the default values: learning rate 10^{-4} , beta_1 = 0.9, and beta_2 = 0.999. The batch size was 10 and the number of epochs was 150.

2.2.3 Evaluation of trained U-Net model accuracy for MC-calculated and measured luminescence images for protons or carbon ions

To evaluate the accuracy of the U-Net model, we predicted 2D-dose distributions from 600 MC-calculated luminescence images of protons or carbon ions. These MC-calculated luminescence images were obtained for testing data: three types of irradiated energy and 200 different lens positions. Moreover, we calculated the root mean square percentage error (RMSPE) and structural similarity index (SSIM) [26] between the MC-calculated dose distributions and U-Net predicted dose distributions or MC-calculated luminescence images for the evaluation of the U-Net model's accuracy for protons or carbon ions on 600 testing image

data. In addition, we selected three representative data in the testing data of the protons or carbon ions to show the MC-calculated luminescence images, MC-calculated dose distribution, U-Net predicted dose distributions, depth profiles, and relative differences for each depth. We measured these depth profiles by setting the image profiles with widths of 20 pixels (~20.8 mm). All depth profiles were normalized to be the same value for the area under the curve. We calculated the relative difference for each depth and the RMSPE between the MC-calculated dose distributions and the U-Net predicted dose distributions as well as between the MC-calculated dose distributions and the MC-calculated luminescence images. The ranges and widths in full width at half maximum (FWHM) of the protons and carbon ions for the U-Net predicted dose distributions as well as the MC-calculated luminescence images were also evaluated and compared with those of the MC-calculated dose distributions.

We conducted the above procedures to apply to the measured luminescence images with three different energies of protons or carbon ions. These luminescence images were measured by the optical method at the Nagoya Proton Therapy Center [23] and Hyogo Ion Beam Medical Center. The irradiated energies used for measurement were 71.6 MeV, 100.2 MeV, and 139.3 MeV for protons, and 190 MeV/u, 216 MeV/u, and 241.5 MeV/u for carbon ion. The original depth of the luminescence images measured by the CCD camera was 16-bit and after the subtraction process of the blank image, these images became 32 bits. We used these 32bit images for the evaluations.

3. Results

3.1 Evaluation of trained U-Net model's accuracy for calculated and measured luminescence images of protons

3.1.1 Estimation of dose distributions of protons from MC-calculated luminescence images

Table 1 summarizes the evaluated results of the similarities of the U-Net predicted dose distributions derived from the MC-calculated luminescence images compared with the MC-calculated dose distributions, and the MC-calculated luminescence images compared with the MC-calculated dose distributions for protons. The RMSPE of the U-Net predicted dose distributions was much smaller, and the SSIM was much larger, than those of the MC-calculated luminescence images. The range and width differences from the MC-calculated dose distributions were slightly improved for the U-Net predicted dose distributions. The time needed to predict one image after training the U-Net model was less than 1 sec.

We selected three simulated testing data (70-MeV, 100-MeV, and 140-MeV protons) for demonstrating the difference in the images among the MC-calculated luminescence images, MC-calculated dose distributions, and U-Net predicted dose distributions from the MC-calculated luminescence images for protons. One of the MC-calculated luminescence images (140-MeV) is shown in Fig. 2 (A), the corresponding MC-calculated dose distributions in Fig. 2 (B), and the U-Net predicted dose distribution from the MC-calculated luminescence images in Fig. 2 (C). In Fig. 2 (D), we show the difference image between the U-Net predicted dose distribution and the MC-calculated dose distribution.

The depth profiles of the MC-calculated luminescence images, MC-calculated dose distributions, and U-Net predicted dose distributions from the MC-calculated luminescence images are plotted for 70-MeV, 100-MeV, and 140-MeV protons and shown in the upper parts of Fig. 3 (A), (B), and (C), respectively. We note that the U-Net predicted dose distributions and dose curves nealy overlap. We also show the relative differences between the dose and U-Net predicted dose distributions or the MC-calculated luminescence images for 70-MeV, 100-MeV, and 140-MeV protons in the lower parts of Fig. 3 (A), (B), and (C), respectively.

The RMSPE values of the profile between the U-Net predicted dose distributions from the MC-calculated luminescence images and MC-calculated dose distributions were 0.54%, 0.70%, and 0.44% for the 70-MeV, 100-MeV, and 140-MeV protons, while those between the MC-calculated luminescence images and

MC-calculated dose distributions were 3.30%, 3.01%, and 2.72% for the 70-MeV, 100-MeV, and 140-MeV protons, respectively.

3.1.2 Estimation of dose distributions of protons from measured luminescence images

We produced the U-Net predicted dose distributions for three measured luminescence images (71.6-MeV, 100.2-MeV, and 139.3-MeV protons). We show one of the measured luminescence images (139.3-MeV) during the irradiation of protons in Fig. 4 (A), the MC-calculated dose distributions in Fig. 4 (B), the U-Net predicted dose distribution from measured luminescence images in Fig. 4 (C), and the difference image of the U-Net predicted and MC-calculated dose distributions in Fig. 4 (D).

The RMSPE and SSIM for the three measured luminescence images and U-Net predicted dose distributions from the measured luminescence images compared with MC-calculated dose distributions are summarized in Table 2. The RMSPEs of the U-Net predicted dose distributions were much smaller, and the SSIMs were much larger, than those of the measured luminescence images. Most of the range and width differences from the MC-calculated dose distributions were slightly improved for the U-Net predicted dose distributions.

The depth profiles for the measured luminescence images, dose distribution, and U-Net predicted dose distributions are plotted for the 71.6-MeV, 100.2-MeV, and 139.3-MeV protons in the upper parts of Fig. 5 (A), (B), and (C), respectively, whereas the relative differences are displayed in the lower parts of Fig. 5 (A), (B), and (C). We observed that the U-Net predicted dose distributions from the measured luminescence images and dose curves nearly overlap.

The RMSPE values of the profiles between the U-Net predicted dose distributions from the measured luminescence images and MC-calculated dose distributions were 0.98%, 2.08%, and 1.68% for the 71.6-MeV, 100.2-MeV, and 139.3-MeV protons, while those between the measured luminescence images

and MC-calculated dose distributions were 3.61%, 2.98%, and 4.33% for the 71.6-MeV, 100.2-MeV, and 139.3-MeV protons, respectively.

3.1.3 Estimation of dose distributions of carbon ions from MC-calculated luminescence images

The evaluated results of the similarities of the U-Net predicted dose distributions from the MC-calculated luminescence images compared with MC-calculated dose distributions, and the MC-calculated luminescence images compared with the MC-calculated dose distributions for carbon-ions are summarized in Table 3. The RMSPEs of the U-Net predicted dose distributions were much smaller, and the SSIMs were much larger, than those of the MC-calculated luminescence images. The range and width differences from the MC-calculated dose distributions were slightly improved.

We selected three simulated testing data (190-MeV/u, 215-MeV/u, and 240-MeV/u carbon ions) for demonstrating the accuracy of the U-Net for carbon ions. We show one of the MC-calculated luminescence images of water (240-MeV/u) in Fig. 6 (A), the corresponding MC-calculated dose distribution in Fig. 6 (B), and the U-Net predicted dose distribution from the MC-calculated luminescence image in Fig. 6 (C). In Fig. 6 (D), we show the difference image between predicted image and MC-calculated dose distribution.

The depth profiles for the MC-calculated luminescence images, dose distribution, and U-Net predicted dose distributions from the MC-calculated luminescence images are plotted for the 190-MeV/u (A), 215-MeV/u (B), and 240-MeV/u (C) carbon ions in the upper parts of Fig. 7 (A), (B), and (C), respectively, whereas the relative differences are plotted in the lower parts of Fig. 7 (A), (B), and (C). We observed that the U-Net predicted dose distributions and dose curves nealy overlap.

The RMSPE values of the profiles between the U-Net predicted dose distributions from the MC-calculated luminescence images and MC-calculated dose distributions were 0.807%, 0.874%, and 0.648%, while those between the MC-calculated luminescence images and MC-calculated dose

distributions were 4.00%, 5.87%, and 11.0% for 190-MeV/u, 215-MeV/u, and 240-MeV/u carbon ions, respectively.

3.1.4 Estimation of dose distributions of carbon ions from measured luminescence images

We produced the U-Net predicted dose distributions for three measured luminescence images (190-MeV/u, 216-MeV/u, and 241.5-MeV/u carbon ions). We show one of the measured luminescence images (241.5-MeV/u) during irradiation of carbon ions in Fig. 8 (A), the MC-calculated dose distributions in Fig. 8 (B), the U-Net predicted dose distribution from the measured luminescence image in Fig. 8 (C), and the difference image between the U-Net predicted and MC-calculated dose distributions in Fig. 8 (D).

The RMSPE and SSIM for the measured luminescence images and the U-Net predicted dose distributions from the measured luminescence images compared with the MC-calculated dose distributions are summarized in Table 4. The RMSPEs of the U-Net predicted dose distributions were much smaller, and the SSIMs were much larger, than those of the measured luminescence images. Most of the range and width differences from the MC-calculated dose distributions improved slightly.

The depth profiles for the measured luminescence images, dose distribution, and U-Net predicted dose distributions from the measured luminescence images are plotted for the 190-MeV/u, 216-MeV/u, and 241.5-MeV/u carbon ions in the upper parts of Fig. 9 (A), (B), and (C), respectively, whereas the relative differences are shown in the lower parts of Fig. 9 (A), (B), and (C). We observed that the U-Net predicted dose distributions and dose curves nealy overlap.

The RMSPE values of the profile between the U-Net predicted dose distributions from the measured luminescence images and MC-calculated dose distributions were 1.70%, 1.19%, and 1.05%, while those between the measured luminescence images and MC-calculated dose distributions were 4.72%, 5.59%, and 8.87% for the 190-MeV/u, 216-MeV/u, and 241.5-MeV/u carbon ions, respectively.

4. Discussion

We successfully predicted 2D-dose distributions from luminescence images of water distorted by the contamination of Cerenkov light using a trained U-Net model. All of the predicted images by the U-Net model showed shapes similar to the MC-calculated dose distributions and demonstrated better accuracy for RMSPE and SSIM as listed in Tables 1-4. Around the Bragg peak region, the relative differences between the U-Net predicted dose distributions and MC-calculated dose distributions showed high values as shown in Figs. 3, 5, 7, and 9. These errors were caused by the small difference in the depth position of the Bragg peak. Except around the Bragg peak region, the relative differences were small and the RMSPE and SSIM were much improved. These results suggest that our methods can accurately and precisely predict dose distributions from the measured luminescence image during the irradiation of protons or carbon ions.

The time needed to produce a single U-Net predicted dose distribution was less than 1 sec, although it took more than 1 day with the Monte Carlo simulation-based conventional correction method [15]. This is good motivation to use the proposed method in routine quality assurance (QA). By including the developed algorithm in our optical imaging system for the luminescence of water, we can achieve almost real-time acquisition of relative dose distributions.

The accuracy of the U-Net predicted dose distributions for the measured luminescence images was slightly worse than those for the MC-calculated luminescence images. The main reason was the difference between the measured images and the MC-calculated luminescence images. Because the MC-calculated luminescence images did not include parallax errors, the Bragg peak heights were slightly lower than those of the measured images [15]. Incorporating the parallax errors in the simulation to produce more realistic training data may improve the accuracy of the U-Net predicted results for the measured luminescence images.

In this study, images predicted by the U-Net model did not show the absolute dose values because all training data were normalized to the maximum intensity for each image. However, it is also important to predict the absolute dose for QA. The intensity of the measured luminescence image of water for X-ray and protons linearly increased with their energies [27]. It will be possible in the future to prepare the training data for different numbers of irradiated particles and to predict the absolute dose according to the intensities of the measured luminescence images of water.

The luminescence image data used in this study were simulated or measured during the irradiation of mono-energetic proton or carbon-ion beams. The DCNN model described in this paper is valid only for various incident energies of protons and carbon ions. Any deviation from these measurement conditions, including deviation from normal beam incident direction and number of irradiated particles, change in water phantom size or shape, or alteration of spot size via the collimator, would require preparation of new training data and retraining for new Monte Carlo simulation data.

After some modifications and preparation of new training data, the DCNN model described in this paper could be applied to other types of luminescence or Cherenkov-light imaging data. One possible application would be the prediction of the dose distributions from the luminescence images of protons for a spread-out Bragg peak (SOBP) [28]. The obtained depth or lateral profiles of the SOBP luminescence images of protons differed from the dose distributions by the Cerenkov light of secondary electrons from prompt gamma photons [28]. For these distorted luminescence images, our method using DCNN has the potential to predict precise dose distribution after training the images for SOBP. Another candidate application for DCNN would be the prediction of the dose distributions from the raw images of Cerenkov light during irradiation of water for high-energy photons or electrons from linear accelerators (LINAC). The raw images of Cerenkov light showed different depth profiles from the dose distributions due to the angular dependency of Cerenkov light [29–33]. For these distorted Cherenkov-light images from a LINAC, our

method using DCNN also has the potential to predict precise dose distribution after training the DCNN using the image data for LINAC.

Scintillator-based optical imaging for protons suffers from the quenching effect depending on the linear energy transfer (LET), as well as the difference in density from that of water [34-36]. To derive the dose distributions, we need to correct scintillation images for the quenching effect and density difference. The DCNN-based correction method may also be able to predict precise dose distributions for liquid scintillator-based optical imaging.

5. Conclusions

We successfully predicted two-dimensional dose distributions from the measured as well as MC-calculated luminescence images of water for protons and carbon ions using the U-Net model. Using our DCNN, the average RMSPE values decreased from 4.38% to 1.38%, while the average SSIM values increased from 0.657 to 0.964. The proposed method has the potential to improve the accuracy of relative 2D-dose distribution for proton or carbon-ion beams.

Acknowledgements

We performed this study's proton experiments and carbon-ion measurements at the Nagoya Proton Therapy Center and Hyogo Ion Beam Medical Center, respectively. We thank the clinical teams for granting us beam time for our experiments and the staffs who helped us prepare and carry out the irradiations. This work was supported in part by JSPS KAKENHI 18K19909.

Conflict of Interest Statement

The authors declare no conflicts of interest associated with this manuscript.

References

- [1] Hishikawa Y, Kagawa K, Murakami M, Sakai H, Akagi T, and Abe M, Usefulness of positron-emission tomographic images after proton therapy, *Int. J. Radiation Oncology Biol. Phys.*, vol. 53, pp. 1388-1391, 2002.
- [2] Parodi K, Enghardt W, and Haberer T, In-beam PET measurements of radioactivity induced by proton beams, *Phys. Med. Biol.*, vol. 47, pp. 21-36, 2002.
- [3] S. Yamamoto, T. Toshito, M. Komori, Y. Morishita, S. Okumura, M. Yamaguchi, Y. Saito, N. Kawachi, S. Fujimaki., Monitoring of positron using high-energy gamma camera for proton therapy. *Ann Nucl Med.* Apr;29(3):268-75, 2015.
- [4] Nishio T, Ogino T, Nomura K, and Uchida U, Dose-volume delivery guided proton therapy using beam on-line PET system, *Med. Phys.*, vol. 33, p. 41907, 2006
- [5] C H Min, C H Kim, M Youn and J Kim 2006, Prompt gamma measurements for locating dose falloff region in proton therapy, *Appl. Phys. Lett.* 89 183517.
- [6] Smeets J, Roellinghoff F, Prieels D, Stichelbaut F, Benilov A, Busca P, Fiorini C, Peloso R, Basilavecchia M, Frizzi T, Dehaes JC, Dubus A. Prompt gamma imaging with a slit camera for real-time range control in proton therapy. *Phys Med Biol.*;57(11):3371-405, 2012
- [7] M. Yamaguchi, K. Torikai, N. Kawachi, H. Shimada, T. Satoh, Y. Nagao, et al. Beam range estimation by measuring bremsstrahlung. *Phys. Med. Biol.* 57, 2843-56, 2012.

- [8] S. Yamamoto, M. Yamaguchi, T. Akagi, M. Sasano and N. Kawachi, Development of a YAP(Ce) camera for the imaging of secondary electron bremsstrahlung x-ray emitted during carbon-ion irradiation toward the use of clinical conditions, *Phys. Med. Biol.* 64 (2019) 135019 (15pp)
- [9] Hayakawa Y, Tada J, Arai N, Hosono K, Sato M, Wagai T, Tsuji H and Tsuji H 1995 Acoustic pulse generated in a patient during treatment by pulsed proton radiation beam *Radiat. Oncol. Invest.* 3 42–5
- [10] James R, Eleanor M, Ben C and Bradley E T 2017 Sensitivity of simulated transcranial ultrasound fields to acoustic medium property maps *Phys. Med. Biol.* 62 2559
- [11] S. Yamamoto, T. Toshito, S. Okumura, and M. Komori, Luminescence imaging of water during proton-beam irradiation for range estimation, *Med. Phys.* 42 (11), 6498–6506, 2015
- [12] S. Yamamoto, M. Komori, T. Akagi, T. Yamashita, S. Koyama, Y. Morishita, E. Sekihara, and T. Toshito, Luminescence imaging of water during carbon-ion irradiation for range estimation, *Med. Phys.* 43 (5), 2455–2463, 2016
- [13] S. Yamamoto, T. Akagi, T. Yamashita, J. Toivonen, M. Yamaguchi, M. Komori, and N. Kawachi, Source of luminescence of water lower energy than the Cerenkov-light threshold during irradiation of carbon-ion, *Journal of Physics Communications*, 2, 065010, 2018
- [14] Yabe, T., Sasano, M., Hirano, Y., Toshito, T., Akagi, T., Yamashita, T., Hayashi, M., Azuma, T., Sakamoto, Y., Komori, M., & Yamamoto, S. (2018). Addition of luminescence process in Monte Carlo simulation to precisely estimate the light emitted from water during proton and carbon-ion irradiation. *Physics in Medicine and Biology*, 63(12).
- [15] T. Yabe, M. Komori, T. Toshito, M. Yamaguchi, N. Kawachi, and S. Yamamoto, Estimation and correction of produced light from prompt gamma photons on luminescence imaging of water for proton therapy dosimetry, *Phys. Med. Biol.* 63 (4), 04NT02, 2018

- [16] D. Hwang, K. Y. Kim, S. K. Kang, S. Seo, J. C. Paeng, D. S. Lee, and J. S. Lee, Improving the accuracy of simultaneously reconstructed activity and attenuation maps using deep learning, *J. Nucl. Med.* 59 (10), 1624–1629, 2018
- [17] D. Hwang, S. K. Kang, K. Y. Kim, S. Seo, J. C. Paeng, D. S. Lee, and J. S. Lee, Generation of PET attenuation map for whole-body time-of-flight ^{18}F -FDG PET/MRI using a deep neural network trained with simultaneously reconstructed activity and attenuation maps, *J. Nucl. Med.* 60 (8), 1183–1189, 2019
- [18] W. Whiteley and J. Gregor, CNN-based PET sinogram repair to mitigate defective block detectors, *Phys. Med. Biol.* 64 (23), 235017, 2019
- [19] G. Zaharchuk, Next generation research applications for hybrid PET/MR and PET/CT imaging using deep learning, *Eur. J. Nucl. Med. Mol. Imaging* 46 (13), 2700–2707, 2019
- [20] Z. Li, Y. Wang, Y. Yu, K. Fan, L. Xing, and H. Peng, Technical Note: Machine learning approaches for range and dose verification in proton therapy using proton-induced positron emitters, *Med. Phys.* 46 (12), 5748–5757, 2019
- [21] C. Liu, Z. Li, W. Hu, L. Xing, and H. Peng, Range and dose verification in proton therapy using proton-induced positron emitters and recurrent neural networks (RNNs), *Phys. Med. Biol.* 64 (17), 175009, 2019
- [22] C.-C. Liu and H.-M. Huang, A deep learning approach for converting prompt gamma images to proton dose distributions: A Monte Carlo simulation study, *Phys. Med.* 69, 110–119, 2019
- [23] T. Toshito, C. Omachi, Y. Kibe, et al., A proton therapy system in Nagoya Proton Therapy Center, *Australas Phys. Eng. Sci. Med.* 39 (3), 645–654, 2016
- [24] J. Allison, K. Amako, J. Apostolakis et al., “Recent developments in Geant4”, *Nucl. Instrum. Meth. A* 835; 186-225, 2016

- [25] O. Ronneberger, P. Fischer, and T. Brox, U-net: Convolutional networks for biomedical image segmentation. In: Medical Image Computing and Computer-Assisted Intervention (MICCAI). New York, NY: Springer; 2015:234–241
- [26] Z. Wang, A.C. Bovik, H. R. Sheikh, and E. P. Simoncelli, Image quality assessment: from error visibility to structural similarity. *IEEE Transactions on Image Processing*. Apr; 13(4):600-12, 2004.
- [27] S. Yamamoto, S. Koyama, T. Yabe, M. Komori, J. Tada, S. Ito, T. Toshito, Y. Hirata, and K. Watanabe, Stability and linearity of luminescence imaging of water during irradiation of proton-beams and X-ray photons lower energy than the Cerenkov light threshold, *Nuclear Inst. and Methods in Physics Research Section A* 883 (1), 48–56, 2018
- [28] M. Komori, E. Sekihara, T. Yabe, R. Horita, T. Toshito, and S. Yamamoto, Luminescence imaging of water during uniform-field irradiation by spot scanning proton beams, *Phys. Med. Biol.* 63 (1), 1–8, 2018
- [29] A. K. Glaser, S. C. Davis, D. M. McClatchy, R. Zhang, B. W. Pogue, and D. J. Gladstone, Projection imaging of photon beams by the Cerenkov effect, *Med. Phys.* 40 (1), 012101, 2013
- [30] A. K. Glaser, S. C. Davis, W. H. Voigt, R. Zhang, B. W. Pogue, and D. J. Gladstone, Projection imaging of photon beams using Cerenkov-excited fluorescence, *Phys. Med. Biol.* 58 (3), 601–619, 2013
- [31] S. Yamamoto, K. Okudaira, F. Kawabata, T. Nakaya, and H. Oguchi, Optical imaging of water during X-ray beam irradiations from linear accelerator, *Nuclear Inst. and Methods in Physics Research Section A* 872 (11), 174–180, 2017
- [32] Y. Helo, I. Rosenberg, D. D'Souza, L. Macdonald, R. Speller, G. Royle, and A. Gibson, Imaging Cerenkov emission as a quality assurance tool in electron radiotherapy, *Phys. Med. Biol.* 59 (8), 1963–1978, 2014
- [33] S. Yamamoto, K. Okudaira, F. Kawabata, T. Nakaya, and H. Oguchi, Imaging of produced light in water during high energy electron beam irradiations from a medical linear accelerator, *Radiat. Meas.* 116, 1–9, 2018

- [34] A. S. Beddar, Plastic scintillation dosimetry and its application to radiotherapy, *Radiat. Meas.* 41 (S1) S124–S133, 2006
- [35] A. S. Beddar, T. R. Mackie, and F. H. Attix, Water-equivalent plastic scintillation detectors for high-energy beam dosimetry: I. Physical characteristics and theoretical consideration, *Phys. Med. Biol.* 37 (10), 1883–1900, 1992
- [36] A. S. Beddar, T. R. Mackie, and F. H. Attix, Water-equivalent plastic scintillation detectors for high-energy beam dosimetry: II. Properties and measurements, *Phys. Med. Biol.* 37 (10), 1901–1913, 1992

Figure legends

Fig. 1 Architecture of U-Net for predicting dose distribution from MC-calculated and measured luminescence images for protons or carbon ions.

Fig. 2 MC-calculated luminescence image for 140-MeV protons (A), corresponding MC-calculated dose distribution (B), U-Net predicted dose distribution from MC-calculated luminescence image (C), and difference image of U-Net predicted dose distribution and MC-calculated dose distribution (D).

Fig. 3 Depth profiles (upper) for MC-calculated luminescence images, dose distribution, and U-Net predicted dose distributions from MC-calculated luminescence images, and relative differences (lower) between MC-calculated dose and U-Net predicted dose distributions or MC-calculated luminescence images for 70-MeV (A), 100-MeV (B), and 140-MeV (C) protons.

Fig. 4 Measured luminescence image for 140-MeV protons (A), corresponding MC-calculated dose distribution (B), U-Net predicted dose distribution from measured luminescence image (C), and difference image of U-Net predicted and MC-calculated dose distributions (D).

Fig. 5 Depth profiles (upper) for measured luminescence images, dose distribution, and U-Net predicted dose distributions from measured luminescence images, and relative differences (lower) between dose and U-Net predicted dose distributions or measured luminescence images for 71.6-MeV (A), 100.2-MeV (B), and 139.3-MeV (C) protons.

Fig. 6 MC-calculated luminescence image for 240-MeV/u carbon ions (A), corresponding MC-calculated dose distribution (B), U-Net predicted dose distribution from MC-calculated luminescence image (C), and difference image of U-Net predicted dose distribution and MC-calculated dose distribution (D).

Fig. 7 Depth profiles (upper) for MC-calculated luminescence images, dose distribution, and U-Net predicted dose distributions, and relative differences (lower) between dose and U-Net predicted dose distributions or MC-calculated luminescence images for 190-MeV/u (A), 215-MeV/u (B), and 240-MeV/u carbon ions.

Fig. 8 Measured luminescence images for 241.5-MeV/u carbon ions (A), corresponding dose (B), U-Net predicted dose distribution from measured luminescence image (C) and difference image of U-Net predicted dose distributions and MC-calculated dose distributions (D).

Fig. 9 Depth profiles (upper) for measured luminescence images, dose distribution, and U-Net predicted dose distributions from measured luminescence images and relative differences (lower) between dose and U-Net predicted dose distributions or measured luminescence images for 190-MeV/u (A), 216-MeV/u (B), and 241.5-MeV/u carbon ions

Table legends

Table 1 Averaged values of RMSPE, SSIM, and differences of ranges and widths of U-Net predicted dose distributions derived from MC-calculated luminescence images or MC-calculated luminescence images compared with the MC-calculated dose distributions for 600 simulated testing data of protons.

Table 2 RMSPE, SSIM, and difference of ranges and widths of U-Net predicted dose distributions from measured luminescence images or measured luminescence images compared with MC-calculated dose distributions for 71.6-MeV, 100.2-MeV, and 139.3-MeV protons.

Table 3 Averaged values of RMSPE, SSIM, and difference of ranges and widths of U-Net predicted dose distributions from MC-calculated luminescence images or MC-calculated luminescence images compared with MC-calculated dose distributions for 600 simulated testing data of carbon ions.

Table 4 RMSPE, SSIM, and difference of ranges and widths for U-Net predicted dose distributions from measured luminescence images and measured luminescence images compared with MC-calculated dose distributions for 190-MeV/u, 216-MeV/u, and 241.5-MeV/u carbon ions.

Table 1

	RMSPE (%)	SSIM	Range difference (mm)	Width difference (mm)
U-Net predicted dose distributions / MC-calculated	0.357 / 2.28	0.992 / 0.793	0.35 / 0.36	0.27 / 0.67
luminescence image				

Averaged values of RMSPE, SSIM, and differences of ranges and widths of U-Net predicted dose distributions derived from MC-calculated luminescence images or MC-calculated luminescence images compared with the MC-calculated dose distributions for 600 simulated testing data of protons.

Table 2

U-Net predicted dose distributions / Measured luminescence images	RMSPE (%)	SSIM	Range difference (mm)	Width difference (mm)
71.6 MeV	1.24 / 2.57	0.928 / 0.632	0.0 mm / -1.0 mm	-1.1 mm / -0.45 mm
100.2 MeV	1.47 / 2.42	0.965 / 0.696	0.0 mm / 0.0 mm	+0.46 mm / +1.5 mm
139.3 MeV	1.68 / 3.41	0.962 / 0.650	-1.0 mm / -2.1 mm	+1.1 mm / +2.0 mm

RMSPE, SSIM, and difference of ranges and widths of U-Net predicted dose distributions from measured luminescence images or measured luminescence images compared with MC-calculated dose distributions for 71.6-MeV, 100.2-MeV, and 139.3-MeV protons.

Table 3

	RMSPE (%)	SSIM	Range difference (mm)	Width difference (mm)
U-Net predicted dose distributions / MC-calculated	0.595 / 3.70	0.994 / 0.813	0.35 / 0.36	0.43 / 0.60
luminescence images				

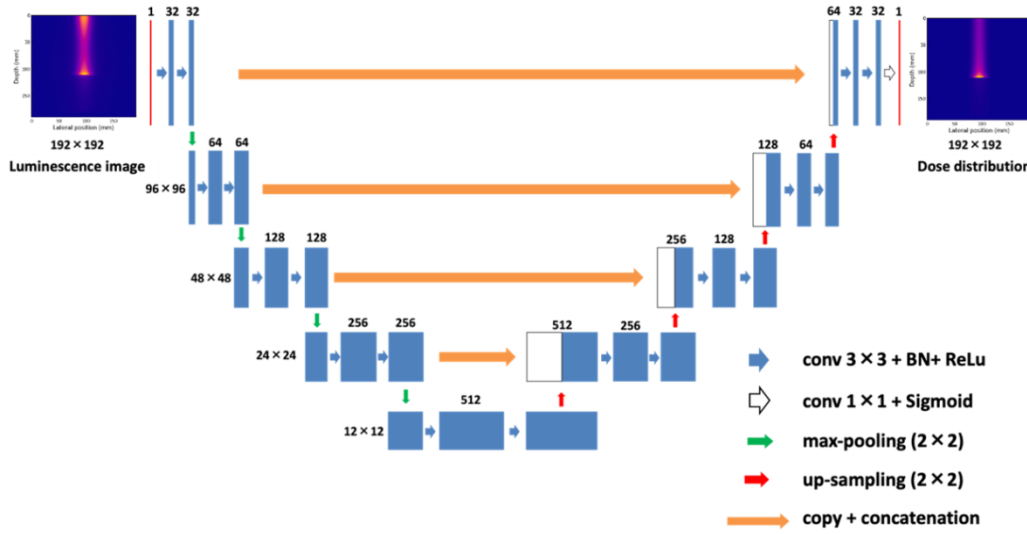
Averaged values of RMSPE, SSIM, and difference of ranges and widths of U-Net predicted dose distributions from MC-calculated luminescence images or MC-calculated luminescence images compared with MC-calculated dose distributions for 600 simulated testing data of carbon ions.

Table 4

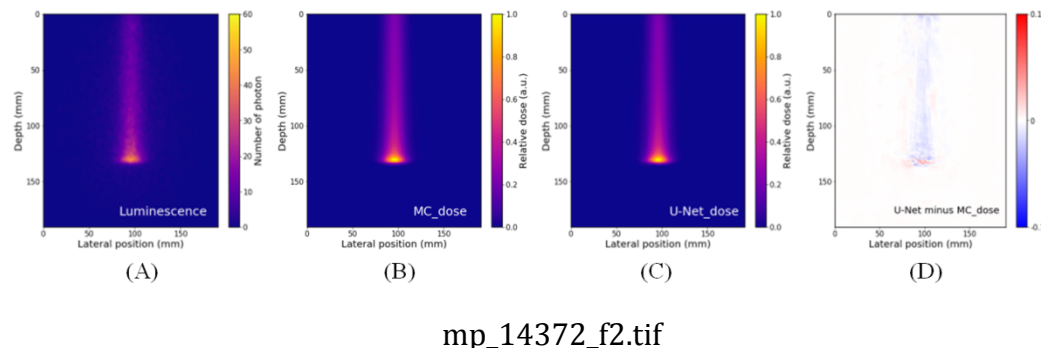
U-Net predicted dose distributions / Measured luminescence images	RMSPE (%)	SSIM	Range difference (mm)	Width difference (mm)
190 MeV/u	1.46 / 5.79	0.968 / 0.577	0.0 mm / 0.0 mm	1.3 mm / 3.1 mm
216 MeV/u	1.14 / 6.16	0.971 / 0.621	0.0 mm / 1.0 mm	1.7 mm / 3.7 mm
241.5 MeV/u	0.878 / 5.93	0.989 / 0.763	1.0 mm / 0.0 mm	1.4 mm / 2.2 mm

RMSPE, SSIM, and difference of ranges and widths for U-Net predicted dose distributions from measured luminescence images and measured luminescence images compared with MC-calculated dose distributions for 190-MeV/u, 216-MeV/u, and 241.5-MeV/u carbon ions.

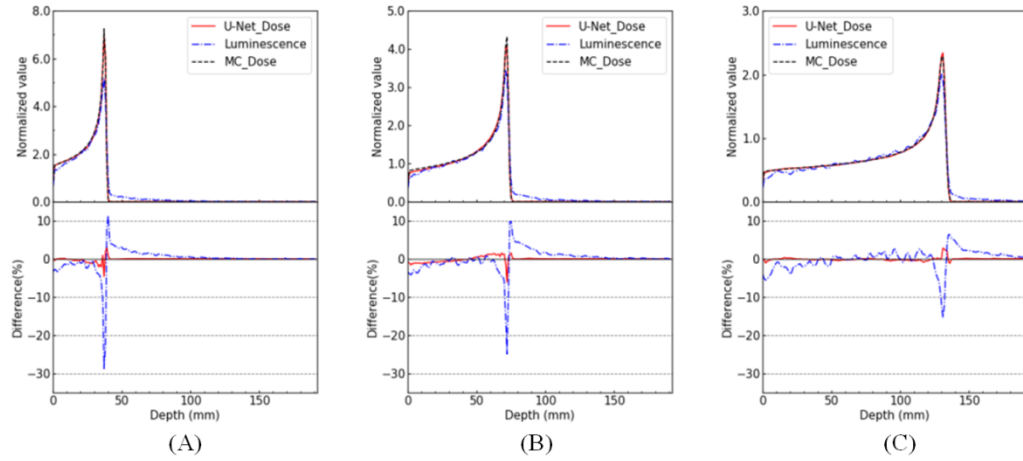
Accepted Article



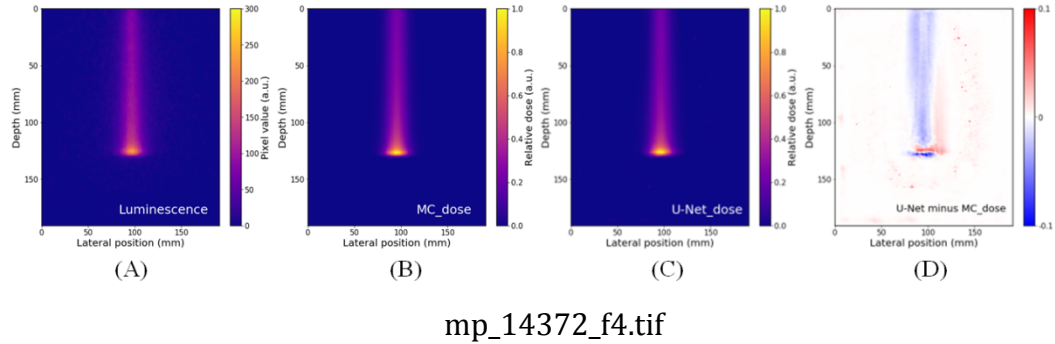
mp_14372_f1.tif



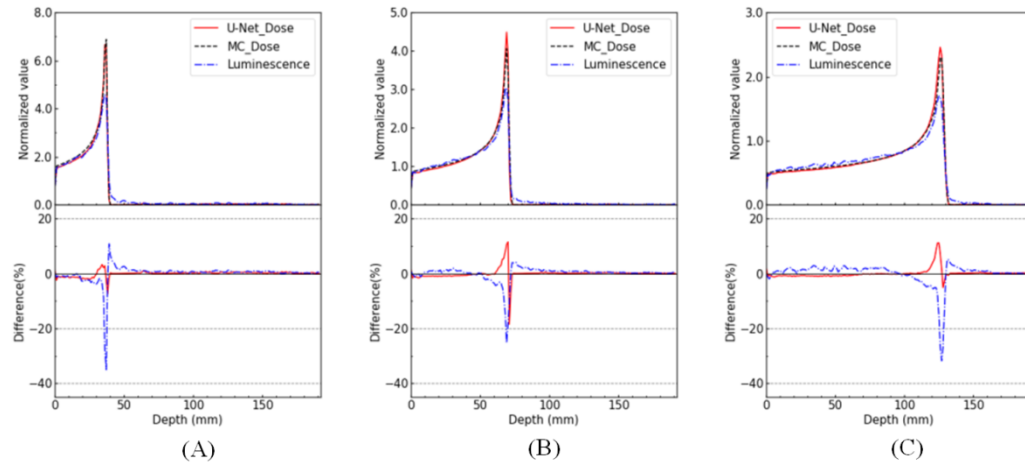
mp_14372_f2.tif



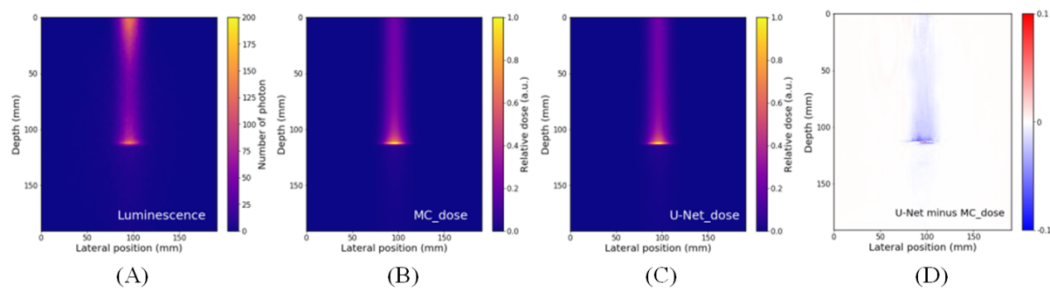
mp_14372_f3.tif



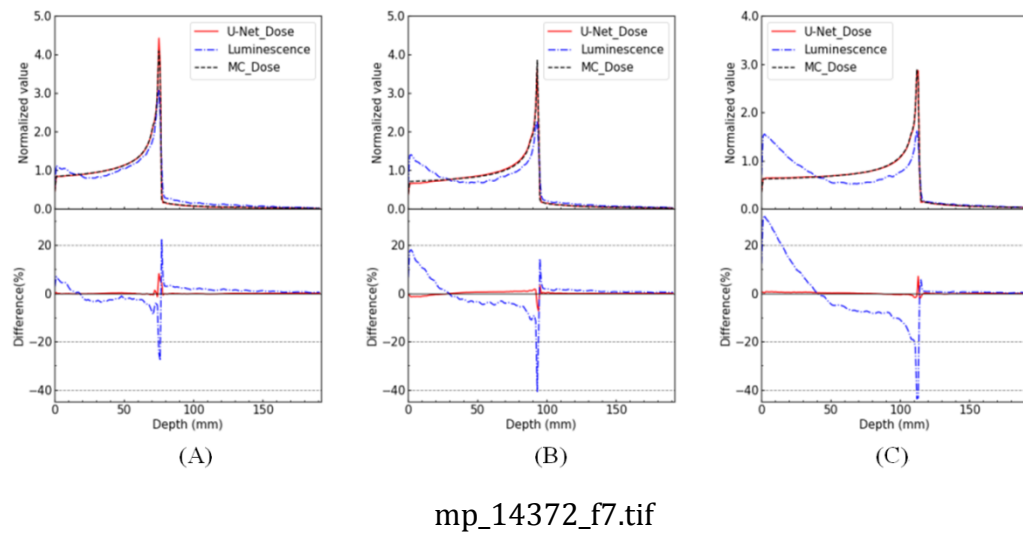
mp_14372_f4.tif



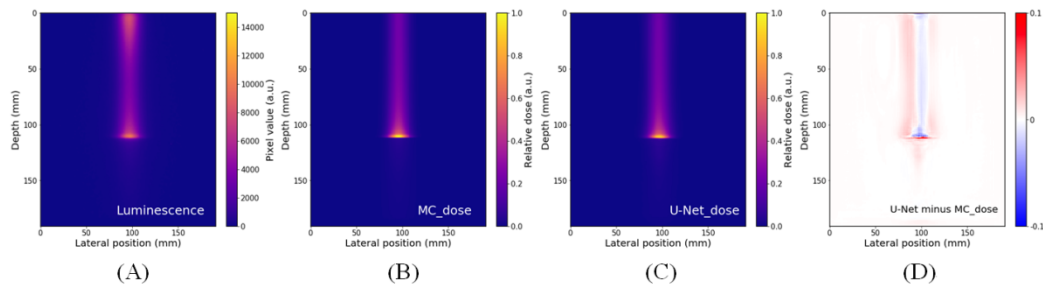
mp_14372_f5.tif



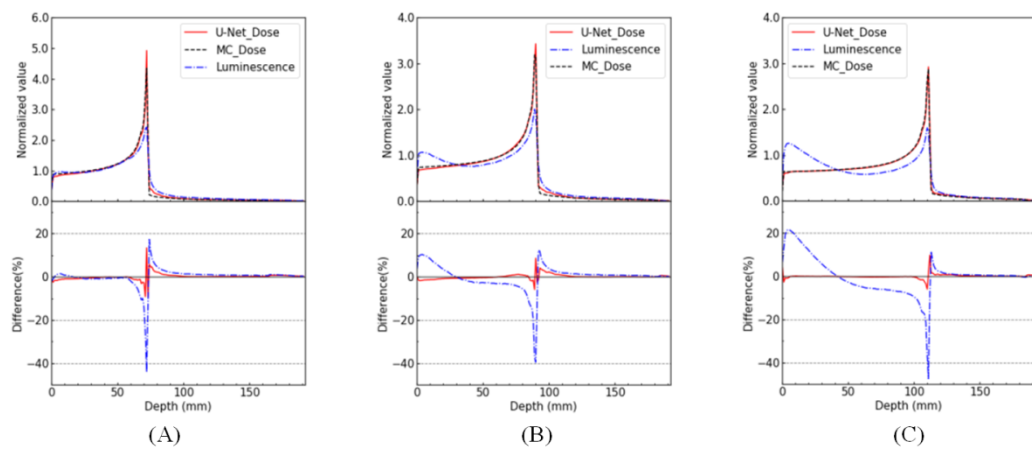
mp_14372_f6.tif



mp_14372_f7.tif



mp_14372_f8.tif



mp_14372_f9.tif